This is the accepted version of the manuscript. For the online version, please visit: https://doi.org/10.1109/JMEMS.2020.3004847

Fabrication of Out-of-Plane High Channel Density Microelectrode Neural Array with 3D Recording and Stimulation Capabilities

Md Mobashir Hasan Shandhi, *Student Member, IEEE,* and Sandeep Negi

***Abstract*—The Utah Electrode Array (UEA) and its different variants have become a gold standard in penetrating high channel count neural electrode for bi-directional neuroprostheses (simultaneous recording and stimulation). However, despite its usage in numerous applications, it has one major drawback of having only one active site per shaft, which is at the tip of the shaft. In this work, we are demonstrating a next-generation device, the Utah Multisite Electrode Array (UMEA), which is capable of having multiple sites around the shaft and also retaining the site at the tip. The UMEA can have up to 9 sites per shaft (hence can accommodate 900 active sites) while retaining the form factor of the conventional UEA with 100 sites. However, in this work and to show the proof of concept, the UMEA was fabricated with one active site at the tip and two around the shaft at different heights; thus, three active sites per shaft. The UMEA device is fabricated using a 3D shadow mask patterning technology, which is suitable for a batch fabrication process for these out-of-plane structures. The UMEA was characterized by in-vitro tests to showcase the electrochemical properties of the shaft sites for bi-directional neuroprostheses in contrast to the traditional tip sites of the standard UEA. The UMEA not only improves the channel density of conventional UEAs and hence can access a larger population of neurons, but also enhances the recording and stimulation capabilities from different layers of the human cortex without further increasing the risk of neuronal damage.**

***Index Terms*—Utah Electrode Array, Utah Multisite Electrode Array, Shadow Mask, Neural Electrodes, Microelectrodes.**

I. Introduction

Neuromodulation techniques (e.g., brain stimulation and peripheral nerve stimulation) are used for the treatment of various neurological conditions, such as Parkinson's disease [1, 2], essential tremor [3, 4], chronic pain [5], epilepsy [6], blindness [7, 8] and is a candidate for improving symptoms of major depressions [9]. On the flip side, neural recordings have enabled us to understand information transfer and processing within the nervous system via recording neural activity (e.g., local field potentials, action potentials, etc.) [10, 11]. Neural electrodes facilitate our ability to both stimulate and record from individual neurons and collections of neurons in-vitro and in-vivo – from a relatively large isolated neuron cell to much smaller neurons in the human cortex [12]. Researchers have advanced these technologies from microwires back in the 1950s [13] to tetrodes in the 90s [14]. In the 1980s and 1990s, silicon microelectrode arrays became the state-of-the-art in the neural electrode field with the advent of silicon micromachining [15, 16]. Recent advancements with flexible substrates brought forth neural electrodes with polymer substrates, equipped with optogenetic capabilities as well [12].

However, silicon microelectrode arrays remain the most common neural electrodes in the chronic recording of neural activities, both for recording action potentials from a single unit and local field potentials from a collection of neurons [12, 17]. The most widely used microelectrode arrays are of two types: the Michigan electrode arrays (MEAs) [18] and the Utah Electrode Arrays (UEAs) [16]. Both of these devices have demonstrated abilities in bi-directional neural interface (simultaneous stimulation and recording) systems, not only with electrical signals [15, 16, 18, 19] but also with optical signals, enabling optogenetics [20, 21].

The advancement of silicon microfabrication techniques has enabled the development and fabrication of these microelectrode arrays with a very small footprint. This has consequently led to reduced neuronal damage and enhanced biocompatibility compared to contemporary neural electrodes [11]. Out of the two families of widely used microelectrode arrays, the MEAs are fabricated using standard planar microfabrication technologies (e.g., dopant diffusion, physical and chemical vapor deposition, photolithography, and etching processes) [15, 18]. These planar probes can then be stacked to form three dimensional (3D) structures if desired [22].

In contrast to the MEAs, the UEAs are fabricated as a 3D device; each typically consists of 10x10 electrically isolated microneedle-shaped electrodes with a 400 μm pitch between the electrodes and one active site per shaft (at the tip of the electrode) [16], as shown in Fig. 1 (a) & (b). The UEAs are produced from thick silicon wafers via a combination of different micromachining and lithography techniques [23]. The length of the microneedles (shafts) varies from 500 μm to 1500 μm [24]. The tips of the silicon needles are then metalized (typically with platinum or iridium oxide) in a sputtering

Research reported in this publication was supported by the National Institute of Neurological Disorders and Stroke of the National Institutes of Health under Award Number R01NS085213. The content is solely the responsibility of the authors and does not necessarily represent the official views of the National Institutes of Health.

M. M. H. Shandhi and S.Negi are with School of Electrical and Computer Engineering. University of Utah, Salt Lake City, UT, USA. Corresponding author email: mobashir.shandhi@gmail.com.

process to improve the electrochemical charge transfer between the device and the surrounding biological media. The entire device is coated with a biocompatible polymer (i.e., Parylene-C), to reduce the foreign body response when implanted and provide electrical isolation. Finally, the electrode sites are formed by removing the Parylene-C encapsulation coating from the upper 30–50 μm of the metalized silicon tips, as shown in Fig. 1(b). Insulated gold wires are wire-bonded to the contact pads on the back of the UEA for each shaft and attached then to a connector. The bond sites are subsequently encapsulated with medical-grade silicone.

Implanted UEAs are connected to a skull-mounted interface with flexible wire bundles and the device floats on the surface of the brain. Due to their relatively large electrode count and large surface area, these devices have become crucial components in studies involving non-human primates [25] as well as human studies [19, 26]. To date, UEA is the only high channel count penetrating neural probe to be approved by the US Food and Drug Administration (FDA) for chronic use in human patients [19].

There are a few different variants of the UEAs available to serve various applications, e.g., standard UEA with constant microneedle length, Utah slant electrode array (USEA), convoluted shape UEAs (with concave and convex curvature), and high-density (HD) UEAs (with a pitch of 200 μm compared to a pitch of 400 μm for the standard UEA) [24]. The USEA and HD-UEA were developed to access different layers of neurons from the same device and to increase the number of active channel counts, respectively [27]. They can address larger portions of the brain and nerve tissue as well as submillimeter neuroanatomical structures, without increasing discomfort and risk of infection for the patient.

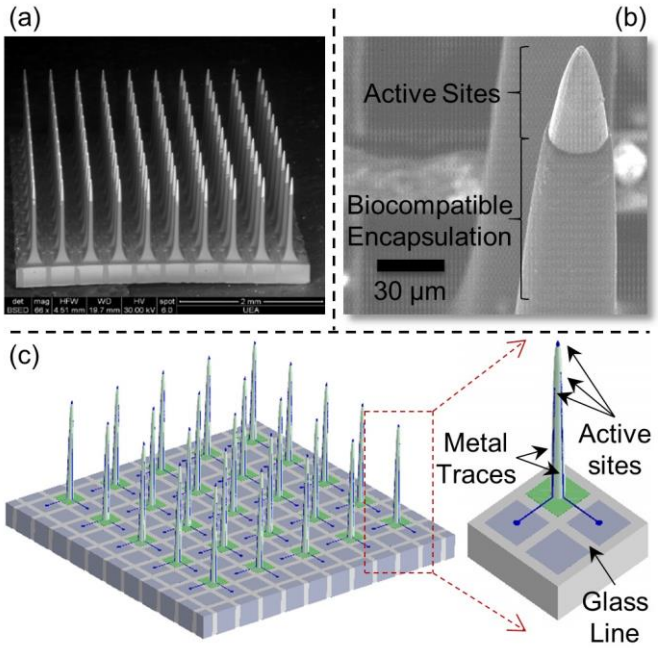

Fig. 1. Scanning electron micrographs of (a) a standard Utah electrode array (UEA) and (b) a single microneedle in the UEA, where the exposed active site is coated with Platinum and the remainder of the device is coated with a biocompatible polymer Parylene-C. (c) Schematics of the Utah Multisite Electrode Array (UMEA) with three active sites per needle for a total of 75 active sites.

However, with all the potential of UEAs, the major limitation remains of a single recording site: at the shaft tip. This leaves much to be desired, as a need exists for additional active sites. Due to its complex 3D geometry and dicing-based fabrication process, it is difficult to use planar microfabrication techniques to increase the number of channel counts, Thus, in our previous work [28], we presented a novel device, the Utah Multisite Electrode Array (UMEA), which has recording sites along and around the microneedle of the standard UEAs. We envisioned that this device could have up to 900 active sites in the same footprint of the standard UEAs with 100 active sites. In our previous work [28], we created isolated sites and metal traces along the shaft of the UMEA devices using laser patterning and focused ion beam (FIB) patterning and metal deposition. The FIB patterning and metal deposition techniques can enable the creation of various metal patterns (e.g. square, circles, ring, etc.) along and around the shafts of the UEA device with reproducible resolution and precise control. Using the FIB techniques, metal patterns, and active sites (on the tip and around the shaft of the UEA) of various shapes and sizes, their number, and location can be varied widely [28].

In spite of the flexibility enabled by the FIB techniques, this is a comparatively slow fabrication process where individual sites need to be written/patterned sequentially. For that reason, this process is comparatively costly and not favorable for a batch fabrication process. To solve this challenge, we are proposing a shadow masking [29] based approach to fabricate the UMEA device:

(1) Using laser ablation and electroplating, a nickel shadow mask is fabricated on top of a sacrificial UEA, which is then dissolved to separate the nickel shadow mask.

(2) The nickel shadow mask is placed on top of a UEA device to deposit desired metal (platinum or iridium oxide) via sputtering process to form sites and traces both at the tip and around the shafts, thus fabricating a UMEA device.

Although with this approach it requires additional fabrication steps compared to the fabrication of standard UEA, it allows batch fabrication of UMEA devices with an increased number of active (stimulation and/or recording) sites in the same footprint of a standard UEA. This method is suitable for batch processing, which can potentially reduce device variability between inter and intra-batch productions.

In this paper, we elucidate in detail the design and fabrication methodologies of a proof-of-concept UMEA device using a shadow masking approach. We then describe the encapsulation procedure of the UMEA device in a biocompatible polymer, Parylene-C, and exposure of the active sites at the tip and around the shaft of the device. Finally, we report in-vitro characterization tests, such as electrical impedance spectroscopy (EIS), cyclic voltammetry (CV), and chronopotentiometry of the UMEA device to showcase the usability of the fabricated device.

II. Design

The UMEA chosen for this proof of concept study has the same footprint as the standard UEA. It has a total of 25 shafts (i.e., 5x5 UEA) and three-electrode sites per shaft: one at the tip of the shaft and two others about 300 μm and 450 μm below the tip, along the shaft, as illustrated in Fig. 1(c). The base area of

This is the accepted version of the manuscript. For the online version, please visit: https://doi.org/10.1109/JMEMS.2020.3004847

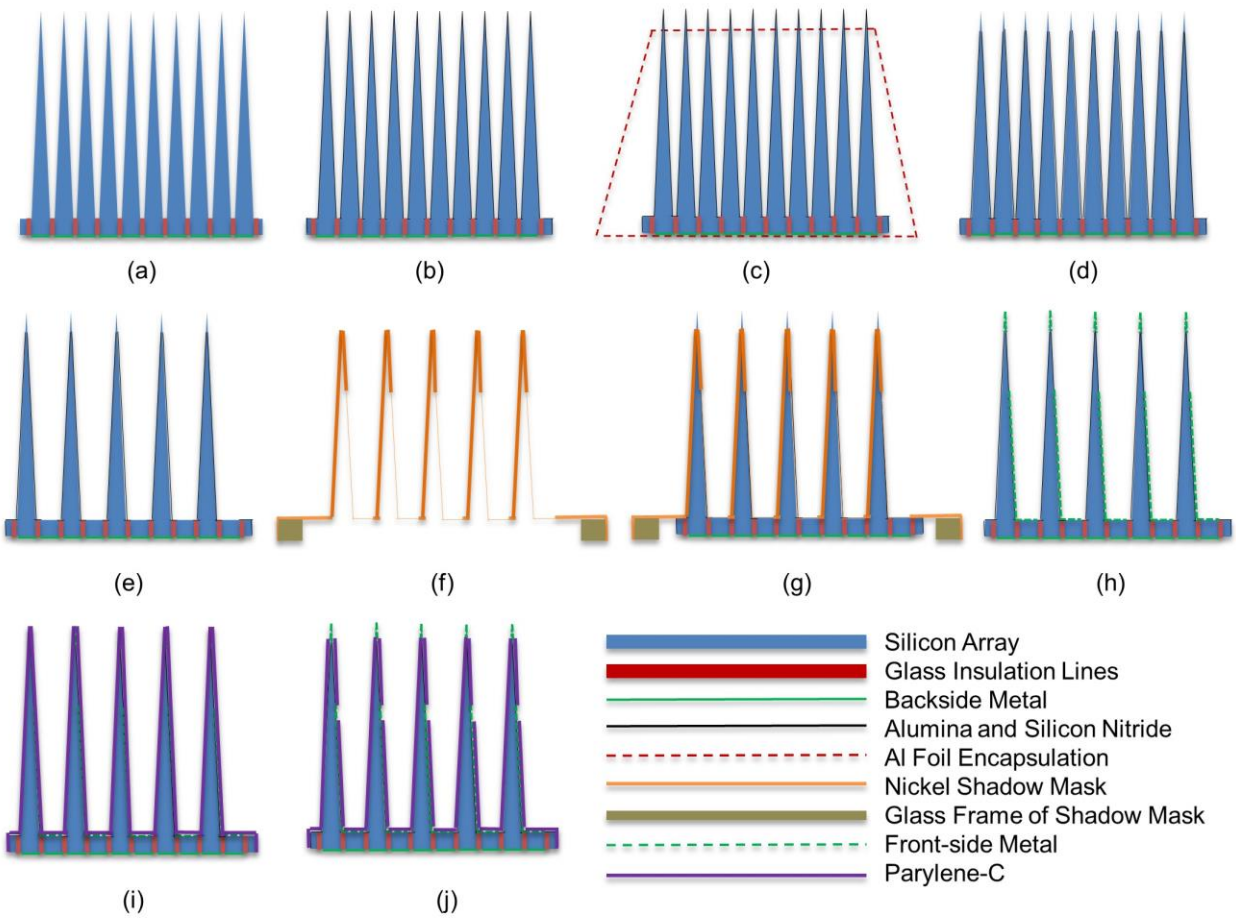

Fig. 2. Fabrication steps of the UMEA device: (a) starting with a 10x10 device with backside bond pads and insulated glass lines among the needles, (b) deposition of Al_2O_3 and silicon nitride insulation layers, (c) aluminum foil encapsulation, (d) etching of silicon nitride layers from the tips, (e) dicing into a 5x5 device, (f) shadow mask, (g) a 5x5 device inside a shadow mask, (h) deposition of front side metal, (i) deposition of parylene-C layer and (j) exposure of active sites..

the device is divided into 100 electrically isolated blocks with glass layers in between them. The highly doped conductive silicon shaft occupies one block and the tip site is connected to the underneath metallic bond pad via the shaft. The sites around the shaft are connected to two neighboring isolated base blocks (and subsequently underneath bonds pads) using the metal traces running down the shaft. Each site on the shaft is electrically isolated from one another using the underlying insulation layer (silicon nitride and alumina) on the shaft. A biocompatible polymer (Parylene-C) is used to coat the device to reduce biotoxicity and foreign body reaction, and aluminum foil punching and laser ablation techniques are used to remove the Parlylene-C layer selectively from the active sites. Finally, a standard connector is wire-bonded to the UMEA device. The design of the corresponding shadow mask is given in [29].

III. Method

A. Fabrication Methodology

Fig. 2 shows the fabrication process flow in a schematic view. It started with a 10x10 UEA followed by the deposition of an insulation layer (Alumina and Silicon Nitride) on the 10x10 UEA device. The insulation layers at the tip of the microneedle were etched to expose the underlying silicon while encapsulating the whole device with an aluminum foil. Then the alternate rows and columns of the microneedle were removed using a dicing process to make the device 5x5, with silicon bases exposed in the empty rows and columns. After that, the device was laid down into a nickel shadow mask [29], and the backside of the device was sealed with glass slides. The device with the shadow mask on top was positioned inside a sputtering chamber to deposit the active sites and metal traces for the sites around the shaft. After the front side metal deposition, the device was encapsulated with a biocompatible polymer Parylene-C and the active sites on the tips were exposed using an aluminum foil pocking technique, as described earlier. The sites around the shaft were exposed using controlled laser ablation. Following the active sites' exposure, the device was connected to a standard connector for in-vitro characterization testing. Each of the fabrication steps is explained in further detail below.

1) Starting 10x10 UEA

The starting 10x10 UEA was fabricated using the steps described in [23]. It had one hundred 1.5 mm long microneedles with a 400 μm pitch between them. It had the backside metallic bond pads and glass lines between the microneedle bases that electrically isolated the microneedles from each other.

2) Alumina Layer Deposition

The sample 10x10 UEA device was ultrasonically cleaned in xylene, N-butyl alcohol (NBA), Isopropyl alcohol (IPA), and deionized (DI) water for 15 minutes, for each process. Following this wet-cleaning step, the sample was cleaned in O_2 plasma in Tehnics-2 for 2 minutes with 100 W of power and O_2 flow of 250 mTorr. Finally, it was cleaned in a buffered oxide etchant (BOE) for 30 seconds to get rid of any oxide. After the cleaning steps, the sample was attached to a glass slide, and the bond pads were protected using a Kapton tape. A thin layer of alumina was deposited using an atomic layer deposition (ALD) process in Cambridge Fiji F200 from water and trimethylaluminum (TMA) precursor. The alumina layer was deposited with 500 ALD cycles at 120°C, and thickness was measured after deposition in Tencor P-10 profilometer. Thickness was found to be 55nm. This conformal layer was deposited to prevent electrical contacts between the front-side metal layer (i.e. metal traces for the shaft sites) and silicon microneedles underneath, through pinholes in the silicon nitride insulation layer (explained in later sections).

3) Silicon Nitride Layer Deposition

Following the alumina layer deposition, a 3-μm thick second layer of insulation (silicon nitride) was deposited using a plasma-enhanced chemical vapor deposition (PECVD) technique for electrical insulation between the active sites (sites at the tip and around the shafts). We used an Oxford Plasmalab 80 PECVD machine with a deposition rate of 25 nm/minute. Gas flow rates were 380 sccm for N_2, 20 sccm for NH_3, and 20 sccm for SiH_4. The deposition pressure and substrate temperature were 1 Torr and 300° C respectively. The deposition process continued for 2 hours and the thickness of the silicon nitride layer was measured later with a film thickness analyzer (Nanospec 3000). The resultant thickness was found to be 3.2 μm.

4) Removal of Silicon Nitride Layer from the Tips

The silicon nitride layer was removed from the tips of the shafts following the work described in [16]. The devices were punched through an aluminum foil, and a package was made around the device, except for the tips. Tip exposure of the shaft was 50 μm. Sample with the package was put in a reactive ion etching (RIE) chamber to etch the silicon nitride from the tips. RIE was carried out for 25 minutes in a mixture of CF_4 and O_2 at 100W of power and 50 mTorr of pressure. Gas flows rates were 35 sccm for CF_4 and 6 sccm for O_2. The alumina layer underneath worked as an etch stop layer. After etching, the aluminum package was removed and verified that it completely removed the Silicon Nitride from the tip, and the underneath alumina layer was exposed.

5) Dicing into 5x5 device

After the removal of silicon nitride from the tips, a Disco dicing saw 3220 was used to remove the alternate rows and columns of the 10x10 UEA device, yielded in a 5x5 device. A 200 μm thick dicing blade (Thermocarbon) was used which involved three cuts with a 100 μm pitch between the cuts to remove one row of shafts. After three cuts were made, the dicing saw was moved a distance of 600 μm to skip one row, and it started cutting the next row of shafts. After a total of 15 cuts were made to remove five rows of shafts, the device was rotated by an angle of 90°, and then another 15 cuts were performed. A total of 75 shafts were removed by these 30 orthogonal cuts (i.e., 15 cuts from two directions), and it resulted in a 5x5 device with an 800 μm pitch between the shafts. The 5x5 device was then cleaned ultrasonically in acetone, IPA, and DI water to get rid of the dicing-dusts. Metal traces running down from the active sites along the shafts were then connected to the backside bond pad through highly doped silicon blocks (described in a later section).

6) Removal of Alumina Layer from the Tip

The exposed alumina layer, at the tip, was removed using BOE. The sample was etched for 40 seconds at 25° C. Inspection showed complete removal of alumina and exposed silicon at the tip.

7) Metal Deposition using Shadow Mask

A front-side metal layer was deposited on the 5x5 device sample with specific pattern transfers using a 3D nickel shadow mask. The shadow mask used for this step is shown in Fig. 3(a). A detailed description of the fabrication of the shadow mask and the metallization process using the shadow mask are given in [29].

Sputtering was used to deposit a layer of 40 nm TiW and 900 nm Pt with TMV super. After the sputtering process, the thickness of the metal was measured using a profilometer (Tencor P-10) and it was found to be 945 nm. After removing the sample from the sputtering chamber, the adhesive of the Kapton tape was removed using xylene. The shadow mask was lifted off the device, and the UMEA device was rinsed in NBA, IPA, and DI water. Fig. 3(b) shows scanning electron micrograph (SEM) images of a device after the sputtering process. The SEM image shows the transferred metal patterns on the UMEA device, with metal at the tip, and metal channels forming metal traces, going down from the shaft to the base. The metal channels in the picture show different pattern widths along the traces; this was due to the gap difference between the UMEA device and shadow mask at various positions on the sample.

8) Parylene-C Layer Deposition

A biocompatible encapsulation layer is required for implanting an invasive neural electrode device. A Paylene-C layer was used as the encapsulation layer for the UMEA device, similar to the standard UEAs [16, 24]. Following the front-side metallization using a shadow mask, the device was coated with Parylene-C using a chemical vapor deposition (CVD) process, following the work reported in [30]. First, an adhesion promoter (Silquest A-174® silane, GE Silicones Inc., WV, USA) was applied on the device before the Parylene-C deposition. Following the application of the promoter, a 3 μm thick Parylene-C layer was deposited using a Paratech 3000 Labtop

This is the accepted version of the manuscript. For the online version, please visit: https://doi.org/10.1109/JMEMS.2020.3004847

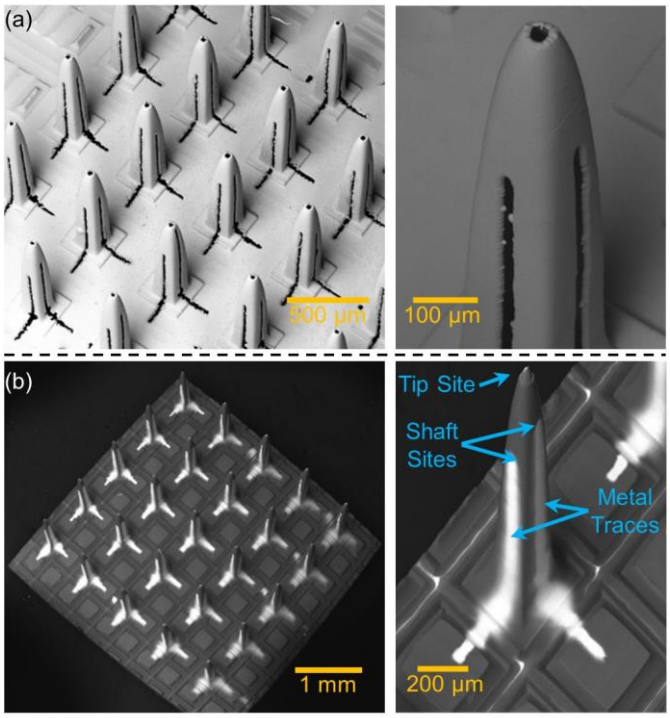

Fig. 3. (a) SEM image of a shadow mask (left) and a patterned hollow needle in the mask (right), (b) SEM image of an UMEA device just after front side metallization through a shadow mask (left) and a zoom in image of a single shaft in the UMEA device (right).

deposition system (Paratech Coating, Inc., CA, USA). The dimer for Parylene-C (Cookson Electronics Equipment, USA) was vaporized at 130°C and subsequently pyrolyzed into reactive monomers at 670°C with a base pressure of less than 10 mTorr set before the dimer sublimation.

9) Parylene-C Layer Removal from the Tip Sites

The Parylene-C encapsulation was removed from the active electrode tips to establish electrical contact between the UMEA device and neural tissue. This is one of the most critical steps, as it defines the active area, called tip exposure. The electrical characteristics and selectivity of the neural device are heavily impacted by the geometrical surface area (GSA) of the electrode tip. It is desired to have a uniform tip exposure throughout the device so that all the electrodes impedance are in a similar range and the recorded signals can be interpreted reliably during in-vivo/vitro testing. In conventional UEA manufacturing, tips are deinsulated using an aluminum foil punching technique where the aluminum foil is used as a mask by poking the microneedles through the foil to the desired exposure with the help of a microscope [16]. We followed the same procedure to expose the tip sites. We used O_2 plasma to etch the Parylene-C layer from the exposed part of the microneedle tip while the aluminum foil protected the rest of the device. After the exposure of the tips sites and plasma clean, the aluminum foil was removed.

10) Parylene-C Layer Removal from the Shaft Sites

An excimer laser (Optec MicroMaster, Optec Laser Systems, San Diego, CA, USA) with a wavelength of 248 nm, was used to expose sites around the shafts. The excimer laser ablated the Parylene-C layer with controlled bursts, and underlying metal sites were exposed. The exposed site diameter was 56 ± 5 µm. Parylene was removed via focusing the demagnified laser spot (spot size of 50 µm in diameter) with laser pulses of 5 ns in duration with a repetition rate of 10 Hz, and laser fluence of 300 mJ/cm^2. Fig. 4 shows the UMEA device with exposed tip and shaft sites.

B. In-vitro Characterization

Following in-vitro characterization tests were performed on the fabricated arrays: (1) EIS, (2) CV, and (3) chronopotentiometry. All three tests are standard and necessary to characterize a neural electrode [31]. EIS provides electrode

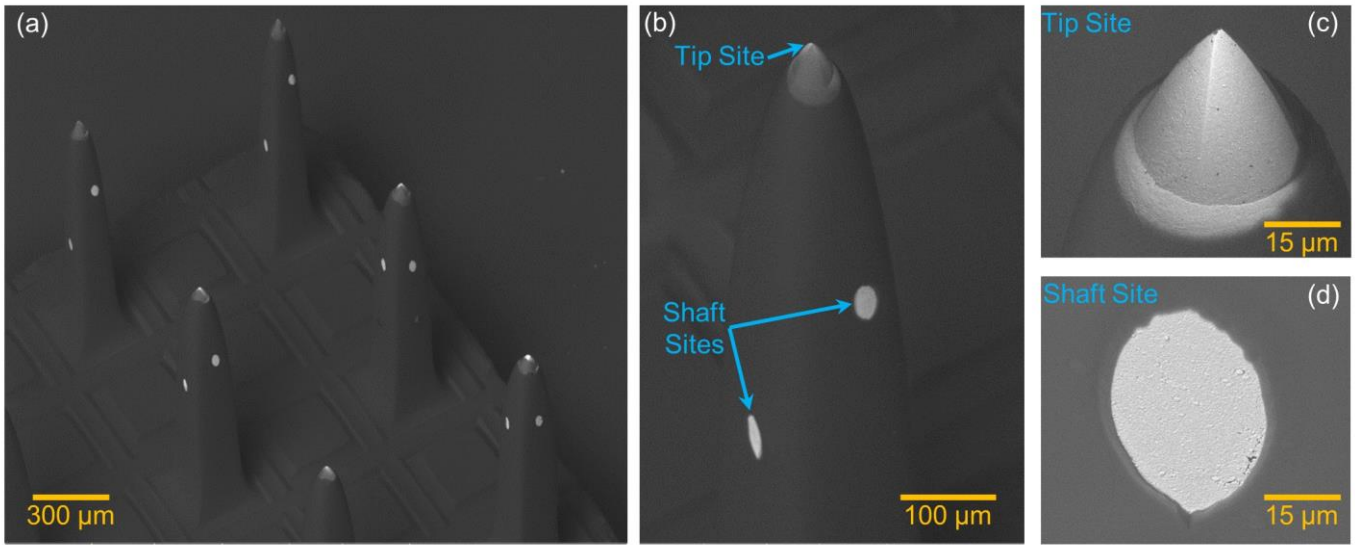

Fig. 4. (a) SEM image of few exposed sites through parylene-C layer on a UMEA device, (b) zoom in image of one shaft with one tip site and two sites around the shaft, (c) zoom in image of a tip site, and (d) zoom in image of a shaft site.

impedance spectra across a frequency range whereas CV and chronopotentiometry are used to gain information regarding the available charge for stimulation by measuring charge-storage capacity (CSC) and charge injection capacity (CIC) of the neural electrode.

The UMEA was immersed in phosphate-buffered saline (PBS) solution at room temperature and performed in-vitro characterization tests at room temperature using a Gamry potentiostat (PC4) testing set, which consisted of an Ag/AgCl reference electrode and a Pt wire as a counter electrode. The details of each test are given below.

1) Electrical Impedance Spectroscopy

For EIS, a sinusoidal signal of 25 mV_{RMS} was applied on the electrode at a frequency range of 10 Hz to 100 kHz. Fig. 6 shows the bode plots of the EIS results for the active sites both at the tips and at the shafts, which reveals the information regarding charge transfer mechanisms for both tip and shaft sites.

2) Cyclic Voltammetry

For CV measurements, we swept the voltage at a rate of 50 mVs^{-1} in the potential range of -0.8 V and 0.8 V. Though most of the CV measurements are performed within -0.6 V to 0.8 V for Pt electrodes [31], however in practice stimulating electrodes are in general operated in a way that may push the potential boundaries [32] to wider ranges. For that reason, we chose a potential boundary of -0.8 V and 0.8 V for the CV. Fig. 7 shows the CV curves for two representative sites, one of the tip sites and one of the shaft sites. From the CV analysis, we calculated CSC values for the active sites both for the sites at the tips and around the shafts, using the following equation:

$$CSC = \frac{1}{\nu A} \int_{E_c}^{E_a} |i| dE \quad (1)$$

Where E = electrode potential, i = measured current, E_a= anodic potential limit, E_c= cathodic potential limit, ν=scan rate of the CV, and A=area of the exposed electrode (which is the GSA of the exposed active sites). The GSA of the tip site is calculated using the following equation, assuming a perfect conic shape [33]:

$$GSA_{Tip-Sites} = \pi r \sqrt{H^2 + r^2} \quad (2)$$

Where r = radius of the base of the cone and H = the height of the cone from the vertex to the center of the base. The GSA of the shaft site is calculated using the following equation, assuming a standard circle:

$$GSA_{Shaft-Sites} = \pi r^2 \quad (3)$$

Where r = radius of the circular opening of the active sites around the shaft. With 50 µm tip exposure for the active sites at the tips, $GSA_{Tip\text{-}Sites}$ were calculated to be approximately $2x10^{-5}$ cm^2 [33]. Similar to the tip sites the $GSA_{Shaft\text{-}Sites}$ were calculated to be approximately $2x10^{-5}$ cm^2 as well, for an active site opening with a radius of 25 µm. We chose the opening radius of the active sites around the shaft to have approximately the same GSA for both the sites at the tip and around the shaft. We further calculated corresponding CSC for both the sites and compared them accordingly.

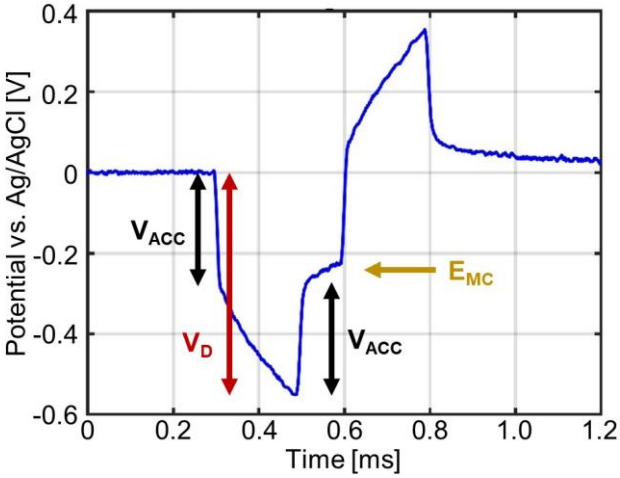

Fig. 5. Voltage transient of an electrode of the UMEA device, illustrating the driving voltage V_D, the access voltage V_{ACC}, and the maximum cathodic potential excursion E_{MC} during a pulse, where E_{MC} is calculated by subtracting V_{ACC} from V_D.

3) Chronopotentiometry

For chronopotentiometry measurement, we applied a current pulse and measured the voltage transients, as shown in Fig. 5. The CIC values were calculated following the works reported in [33], by calculating the stimulating charge from the stimulating current and dividing it by the corresponding GSA for the two types of sites accordingly. Later we compared the two CIC values from the two types of sites to compare their stimulation capabilities.

IV. Results and Discussion

A. Fabrication

Metallization through shadow masks shows a blurring effect of deposited metal on the UMEA device, as shown in Fig. 3(b). Width of the pattern opening on the base and around the shaft of the shadow mask were 40.84 ± 5.02 µm and 39.32 ± 2.98 µm respectively, whereas, the transferred pattern width on the base and around the shaft of the UMEA device were 47.14 ± 5.67 µm and 40.56 ± 3.15 µm respectively. Metal channels in Fig. 3 (b) show different pattern widths along the traces. This was due to the gap difference between the shadow mask and the UMEA device at various positions on the sample, during the sputtering process. Fig. 3(b) shows more blurring effects on the UMEA base compared to metal traces around the microneedle. The gap distance between the shadow mask and UMEA device was more in the base area compared to the microneedle which caused this variation of blurring effects. Future work should focus on fabricating the starting UEA device and shadow mask to have a perfect fit which should minimize the blurring effect significantly.

Blurring is a major limitation in shadow mask based stencil lithography, which precludes its uses in achieving high pattern resolution [34]. In general, researchers use E-beam evaporation in vertical metal transfers via shadow masks rather than sputtering [35], as evaporation has a higher directionality compared to the sputtering process. Hence, it can also potentially decrease the blurring effect even more. However,

the UEA is an FDA approved device, and front-side metallization using sputtering has been used to fabricate the UEA. To keep our metallization process parameters consistent with the standard UEAs, we kept the same sputtering procedure with previously validated parameters [23]. To further check for the effect of the blurring, we tested the UMEA device for electrical shorting between traces. The resistance values between the neighboring traces were over 100 MΩ that indicated no electrical continuity between the neighboring traces. Further investigation and characterization are needed to reduce the blurring effect due to the gap distance of the mask and sample parts at different locations of the device.

After exposing the active sites at both the tip and the shaft, the active sites at the tip showed an opening of 51±8 μm, whereas the active sites around the shaft showed an opening of 56±5 μm in diameter. We also verified the electrical isolation between the sites around the tip and shaft using an electrical shorting test.

Another potential challenge and scope of inter-device variability can result from the laser ablation based deinsulation process of the active sites around the shaft. Advancement in the control systems with precise linear and rotational controllability in novel laser systems should reduce this variability even further. Future work can focus on non-conventional patterning/lithography techniques to open up the active sites around the shaft as well.

An additional note to make here is that the number of actual recording sites is decreased in the UMEA device presented here. After the final step of fabrication, it has 75 active sites compared to 100 active sites of the standard UEA. Theoretically, the method of fabrication presented here can yield an UMEA device with 300 active sites (10x10 device with 3 active sites per microneedle shaft). However, the unavailability of such high channel count connectors would preclude our testing purpose for this device. As we have used a 96 channel connector and for that reason, we chose to fabricate a 5x5 device with 75 actives sites only for this proof of concept study. Future research on new connectors will benefit the connection system of large channel count devices with neural interface systems.

Table 1 summarizes novel microelectrode array-based implantable neuromodulation devices with high-channel counts (more than 100 channels) in comparison to the UMEA device presented here. Almost all of the devices summarized in Table 1 are fabricated using planar photolithography and later stacked together (except mesh electrodes) to increase the number of channel counts, whereas fabrication method for UMEA can increase the number of channel counts in the same footprint of the standard UEA (without increasing the overall geometrical area of the physical structure), which has an inherently non-planar microneedle structure. The proposed method demonstrates the efficacy of using shadow masking based patterning for this kind of high aspect ratio out-of-plane microstructures, which can be translated into novel design and fabrication methodology of neuromodulation devices in future works.

In this work, each microneedle in the UMEA device had only three sites (one at the tip of the microneedle and two around the shaft). Future work should aim for increasing the number of electrode sites, and different design and configuration (e.g. tetrode, hexatrodes, etc.) of electrode sites around the shaft to better sort the neural action potentials which can enhance recording and stimulation capability for high-channel-count devices.

B. In-vitro Characterization

Bode plots of the electrodes are shown in Fig. 6. The tip sites showed an impedance of 81±44 kΩ, whereas the shaft sites showed an impedance of 233±50 kΩ at 1 kHz. These impedance values are comparable with the ones reported in previous work involving standard UEAs [33, 42]. As GSA of both the tip and shaft sites are approximately similar, we believe the difference in the impedance values resulted from the shape of the exposed sites (conical for the tip sites vs. circular for the shaft sites) as well as the cross-sectional area of the conduction path connecting the sites to the bond pads. For example, the tip sites are connected to the underneath bond pads via the heavily doped silicon shaft (with a diameter of approximately 50-100 μm), whereas, the shaft sites are connected to the bond pads via the thin metal traces (with a thickness of approximately 1 μm) running down from the sites towards the base blocks. For neural recording and stimulation applications, the impedance at frequencies around 1 kHz is important as action potentials operate on millisecond time-scales, which is mainly limited by the refractory period [43]. The difference in impedance between the tip and shaft sites becomes very negligible for frequencies > 40 kHz. From the phase plot of Fig. 6(b), the shaft sites show more capacitive behavior compared to the tip sites around 1 kHz.

Fig. 7 shows two representative CV curves, one from a tip site and another one from a shaft site. The shape of the CV curves for both sites is almost similar. The resulted CSC values

TABLE I
COMPARISON OF DIFFERENT HIGH-CHANNEL COUNT IMPLANTABLE MICROELECTRODE ARRAY TECHNOLOGIES

Electrode Technology	Channel Count	Substrate	Fabrication Method	Functionality	References
3D Silicon Probe	1024	Silicon	Planar Microfabrication	Recording Only	Rios et al. 2016 [36]
Neuropixels	960	Silicon	Planar Microfabrication	Recording Only	Jun et al. 2017 [37]
NeuroSeeker	1356	Silicon	Planar Microfabrication	Recording Only	Raducanu et al. 2017 [38]
Mesh Electrode	128	Nanowires	Planar Microfabrication	Recording and Stimulation	Fu et al. 2017 [39]
Polymer Electrode Array	1024	Polyimide	Planar Microfabrication	Recording Only	Chung et al. 2019 [40]
Silicon Microprobe	256	Silicon	Planar Microfabrication	Recording Only	Yang et al. 2020 [41]
UMEA	900*	Silicon	Non-planar Microfabrication	Recording and Stimulation	Current Work

Only arrays with more than 100 channels are considered here.
*By design the UMEA device is capable of having 900 channels, however, current work only shows 75 channels.

This is the accepted version of the manuscript. For the online version, please visit: https://doi.org/10.1109/JMEMS.2020.3004847

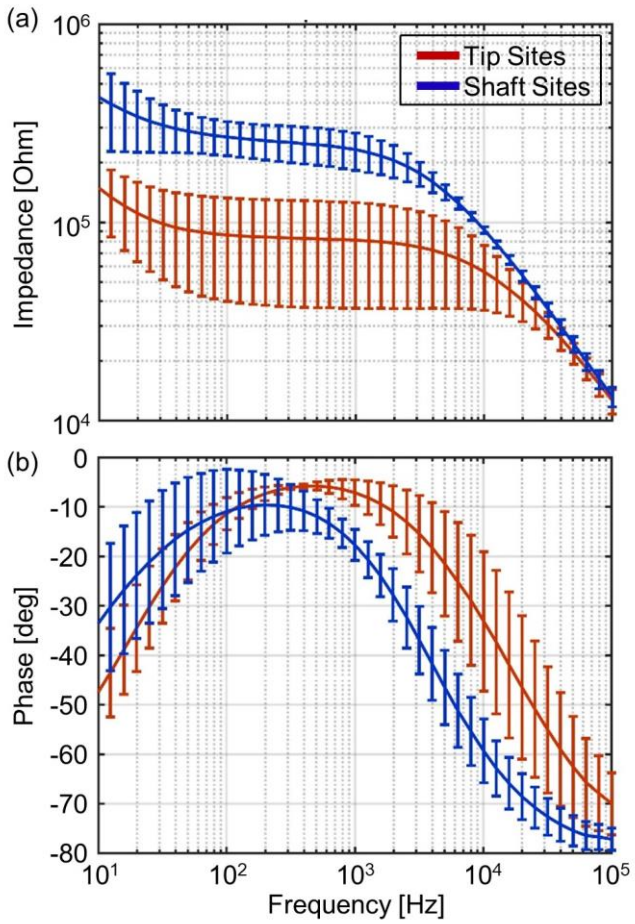

Fig. 6. Bode plots of tip sites and shaft sites on an UMEA device. The curves represent mean values of (a) impedance and (b) phase with standard deviation as error bars.

from the CV tests are 108±38 mC/cm^2 for the tip sites compared to 96±19 mC/cm^2 for the shaft sites. The difference in CSC between tip and shaft sites is not significantly different, though we have seen a significant difference in the impedance. This can be attributed to the fact that the CV scan rate is 50 mV/s which is very slow or pseudo-stationary. During this slow scan, current/charge can be accessed from the total thickness of the platinum layer [31]. Since the thickness of platinum is similar in tip and shaft sites the CSC is also similar. Further characterization is required to understand the effects of shape and size of the shaft sites on the CV curves.

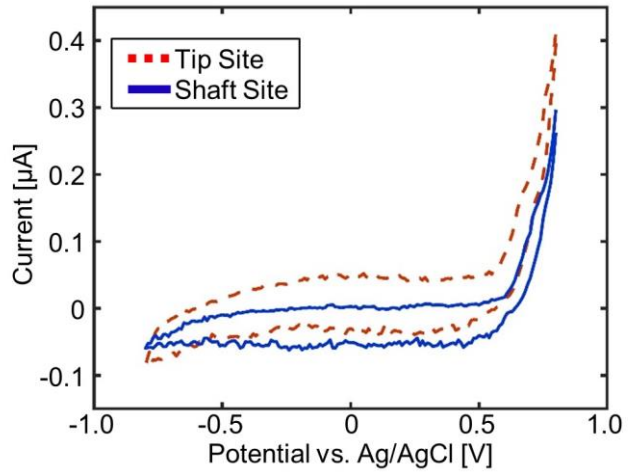

Fig. 7. Representative cyclic voltammograms of one tip site and one shaft site on an UMEA device.

Fig. 8 shows comparative representative voltage transient plots between tip site and shaft site. The CIC at the tip and shaft electrode was calculated to be 0.8 mC/cm^2 and 0.5 mC/cm^2 respectively. The CIC values are consistent with other publications [31-33]. The CIC is higher in the tip electrode compared to the shaft electrode may be due to the 3D geometry of the tip electrodes compared to the planar geometry of the shaft electrodes.

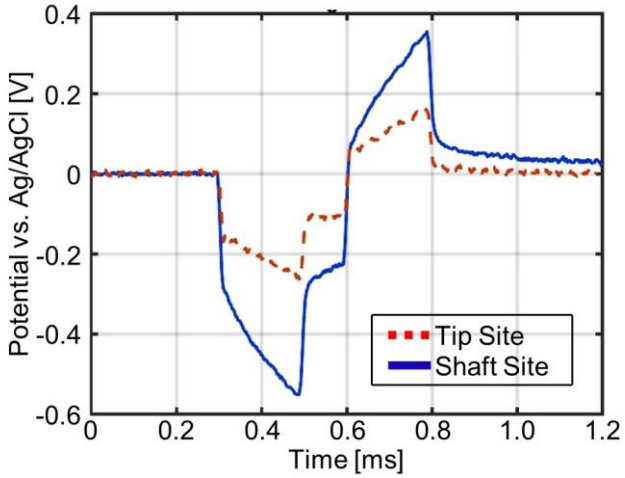

Fig. 8. Representative voltage transient for one tip site and one shaft site of the UMEA device, in response to a biphasic current pulse. The curves are normalized by subtracting the offset idle voltage value at t = 0 s.

All the in-vitro characterization tests showcase the potential of the shaft sites of the UMEA along with the traditional tip sites in neural stimulation and recording. Future in-vivo testing is necessary to verify the applicability and recording/stimulation capability of these devices in acute and chronic studies.

V. Conclusion

In this paper, we presented a fabrication methodology and in-vitro characterization tests of the UMEA device that has three-dimensional recording and stimulation capability. This UMEA has the potential to access multiple layers of the human cortex as well as increase the channel count, which can enable large neuronal mapping. The fabrication methodology presented here can potentially overcome the drawbacks of serial patterning for complex 3D geometries as well. We envision that this method will reduce the overall process time and complexity of building out-of-plane neural electrodes.

Acknowledgment

This work was performed in part at the Utah Nanofab sponsored by the College of Engineering, Office of the Vice President for Research, and the Utah Science Technology and Research (USTAR) initiative of the State of Utah. The authors appreciate the support of the staff and facilities that made this work possible. This work made use of the University of Utah's

shared facilities of the Micron Technology Foundation Inc. Microscopy Suite sponsored by the College of Engineering, Health Sciences Center, Office of the Vice President for Research, and the Utah Science Technology and Research (USTAR) initiative of the State of Utah.

DISCLAIMER

Sandeep Negi has a financial interest in the company Blackrock Microsystems, which develops and produces implantable neural interfaces and electrophysiology equipment and software.

REFERENCES

[1] A.-L. Benabid, P. Pollak, A. Louveau, S. Henry, and J. De Rougemont, "Combined (thalamotomy and stimulation) stereotactic surgery of the VIM thalamic nucleus for bilateral Parkinson disease," *Stereotactic and functional neurosurgery*, vol. 50, no. 1-6, pp. 344-346, 1987.

[2] V. J. Odekerken *et al.*, "GPi vs STN deep brain stimulation for Parkinson disease: three-year follow-up," *Neurology*, vol. 86, no. 8, pp. 755-761, 2016.

[3] J. F. Baizabal-Carvallo, M. N. Kagnoff, J. Jimenez-Shahed, R. Fekete, and J. Jankovic, "The safety and efficacy of thalamic deep brain stimulation in essential tremor: 10 years and beyond," *J Neurol Neurosurg Psychiatry*, vol. 85, no. 5, pp. 567-572, 2014.

[4] A. L. Benabid *et al.*, "Long-term suppression of tremor by chronic stimulation of the ventral intermediate thalamic nucleus," *The Lancet*, vol. 337, no. 8738, pp. 403-406, 1991.

[5] S. G. Boccard *et al.*, "Targeting the affective component of chronic pain: a case series of deep brain stimulation of the anterior cingulate cortex," *Neurosurgery*, vol. 74, no. 6, pp. 628-637, 2014.

[6] R. Fisher *et al.*, "Electrical stimulation of the anterior nucleus of thalamus for treatment of refractory epilepsy," *Epilepsia*, vol. 51, no. 5, pp. 899-908, 2010.

[7] Y. H.-L. Luo and L. Da Cruz, "The Argus® II retinal prosthesis system," *Progress in retinal and eye research*, vol. 50, pp. 89-107, 2016.

[8] L. N. Ayton *et al.*, "First-in-human trial of a novel suprachoroidal retinal prosthesis," *PloS one*, vol. 9, no. 12, p. e115239, 2014.

[9] H. Mayberg, "Deep brain stimulation for treatment-resistant depression," *The American journal of psychiatry*, vol. 167, no. 12, pp. 1437-1444, 2010.

[10] R. Chen, A. Canales, and P. Anikeeva, "Neural recording and modulation technologies," *Nature Reviews Materials*, vol. 2, no. 2, pp. 1-16, 2017.

[11] C. Im and J.-M. Seo, "A review of electrodes for the electrical brain signal recording," *Biomedical Engineering Letters*, vol. 6, no. 3, pp. 104-112, 2016.

[12] G. Hong and C. M. Lieber, "Novel electrode technologies for neural recordings," *Nature Reviews Neuroscience*, vol. 20, no. 6, pp. 330-345, 2019.

[13] F. Strumwasser, "Long-term recording from single neurons in brain of unrestrained mammals," *Science*, vol. 127, no. 3296, pp. 469-470, 1958.

[14] C. M. Gray, P. E. Maldonado, M. Wilson, and B. McNaughton, "Tetrodes markedly improve the reliability and yield of multiple single-unit isolation from multi-unit recordings in cat striate cortex," *Journal of neuroscience methods*, vol. 63, no. 1-2, pp. 43-54, 1995.

[15] K. L. Drake, K. D. Wise, J. Farraye, D. J. Anderson, and S. L. BeMent, "Performance of planar multisite microprobes in recording extracellular single-unit intracortical activity," *IEEE Transactions on Biomedical Engineering*, vol. 35, no. 9, pp. 719-732, 1988.

[16] P. K. Campbell, K. E. Jones, R. J. Huber, K. W. Horch, and R. A. Normann, "A silicon-based, three-dimensional neural interface: manufacturing processes for an intracortical electrode array," *IEEE Transactions on Biomedical Engineering*, vol. 38, no. 8, pp. 758-768, 1991.

[17] G. H. Kim *et al.*, "Recent progress on microelectrodes in neural interfaces," *Materials*, vol. 11, no. 10, p. 1995, 2018.

[18] K. D. Wise, J. B. Angell, and A. Starr, "An integrated-circuit approach to extracellular microelectrodes," *IEEE transactions on biomedical engineering*, no. 3, pp. 238-247, 1970.

[19] L. R. Hochberg *et al.*, "Neuronal ensemble control of prosthetic devices by a human with tetraplegia," *Nature*, vol. 442, no. 7099, pp. 164-171, 2006.

[20] S. Royer, B. V. Zemelman, M. Barbic, A. Losonczy, G. Buzsáki, and J. C. Magee, "Multi-array silicon probes with integrated optical fibers: light-assisted perturbation and recording of local neural circuits in the behaving animal," *European Journal of Neuroscience*, vol. 31, no. 12, pp. 2279-2291, 2010.

[21] J. Zhang *et al.*, "Integrated device for optical stimulation and spatiotemporal electrical recording of neural activity in light-sensitized brain tissue," *Journal of neural engineering*, vol. 6, no. 5, p. 055007, 2009.

[22] K. D. Wise, "Silicon microsystems for neuroscience and neural prostheses," *IEEE engineering in medicine and biology magazine*, vol. 24, no. 5, pp. 22-29, 2005.

[23] R. Bhandari, S. Negi, and F. Solzbacher, "Wafer-scale fabrication of penetrating neural microelectrode arrays," *Biomedical microdevices*, vol. 12, no. 5, pp. 797-807, 2010.

[24] M. Leber *et al.*, "Advances in Penetrating Multichannel Microelectrodes Based on the Utah Array Platform," in *Neural Interface: Frontiers and Applications*: Springer, 2019, pp. 1-40.

[25] M. Yin *et al.*, "Wireless neurosensor for full-spectrum electrophysiology recordings during free behavior," *Neuron*, vol. 84, no. 6, pp. 1170-1182, 2014.

[26] T. Davis *et al.*, "Restoring motor control and sensory feedback in people with upper extremity amputations using arrays of 96 microelectrodes implanted in the median and ulnar nerves," *Journal of neural engineering*, vol. 13, no. 3, p. 036001, 2016.

[27] H. Wark *et al.*, "A new high-density (25 electrodes/mm2) penetrating microelectrode array for recording and stimulating sub-millimeter neuroanatomical structures," *Journal of neural engineering*, vol. 10, no. 4, p. 045003, 2013.

[28] M. Shandhi, M. Leber, A. Hogan, R. Bhandari, and S. Negi, "A novel method of fabricating high channel density neural array for large neuronal mapping," in *2015 Transducers-2015 18th International Conference on Solid-State Sensors, Actuators and Microsystems (TRANSDUCERS)*, 2015: IEEE, pp. 1759-1762.

[29] M. M. H. Shandhi, M. Leber, A. L. Hogan, D. J. Warren, R. Bhandari, and S. Negi, "Reusable high aspect ratio 3-D nickel shadow mask," *Journal of Microelectromechanical Systems*, vol. 26, no. 2, pp. 376-384, 2017.

[30] J.-M. Hsu, L. Rieth, R. A. Normann, P. Tathireddy, and F. Solzbacher, "Encapsulation of an integrated neural interface device with Parylene C," *IEEE Transactions on Biomedical Engineering*, vol. 56, no. 1, pp. 23-29, 2008.

[31] S. F. Cogan, "Neural stimulation and recording electrodes," *Annu. Rev. Biomed. Eng.*, vol. 10, pp. 275-309, 2008.

[32] E. Hudak, J. Mortimer, and H. Martin, "Platinum for neural stimulation: voltammetry considerations," *Journal of Neural Engineering*, vol. 7, no. 2, p. 026005, 2010.

[33] S. Negi, R. Bhandari, L. Rieth, and F. Solzbacher, "In vitro comparison of sputtered iridium oxide and platinum-coated neural implantable microelectrode arrays," *Biomedical materials*, vol. 5, no. 1, p. 015007, 2010.

[34] O. Vazquez-Mena, L. Gross, S. Xie, L. Villanueva, and J. Brugger, "Resistless nanofabrication by stencil lithography: A review," *Microelectronic Engineering*, vol. 132, pp. 236-254, 2015.

[35] J. Brugger, J. W. Berenschot, S. Kuiper, W. Nijdam, B. Otter, and M. Elwenspoek, "Resistless patterning of sub-micron structures by evaporation through nanostencils," *Microelectronic engineering*, vol. 53, no. 1-4, pp. 403-405, 2000.

[36] G. Rios, E. V. Lubenov, D. Chi, M. L. Roukes, and A. G. Siapas, "Nanofabricated neural probes for dense 3-D recordings of brain activity," *Nano letters*, vol. 16, no. 11, pp. 6857-6862, 2016.

[37] J. J. Jun *et al.*, "Fully integrated silicon probes for high-density recording of neural activity," *Nature*, vol. 551, no. 7679, pp. 232-236, 2017.

[38] B. C. Raducanu *et al.*, "Time multiplexed active neural probe with 1356 parallel recording sites," *Sensors*, vol. 17, no. 10, p. 2388, 2017.

[39] T.-M. Fu, G. Hong, R. D. Viveros, T. Zhou, and C. M. Lieber, "Highly scalable multichannel mesh electronics for stable chronic brain electrophysiology," *Proceedings of the National Academy of Sciences*, vol. 114, no. 47, pp. E10046-E10055, 2017.

[40] J. E. Chung *et al.*, "High-density, long-lasting, and multi-region electrophysiological recordings using polymer electrode arrays," *Neuron*, vol. 101, no. 1, pp. 21-31. e5, 2019.

[41] L. Yang, K. Lee, J. Villagracia, and S. C. Masmanidis, "Open source silicon microprobes for high throughput neural recording," *Journal of neural engineering*, vol. 17, no. 1, p. 016036, 2020.

[42] M. Leber, M. Shandhi, A. Hogan, F. Solzbacher, R. Bhandari, and S. Negi, "Different methods to alter surface morphology of high aspect ratio structures," *Applied surface science*, vol. 365, pp. 180-190, 2016.

[43] E. R. Kandel *et al.*, *Principles of neural science*. McGraw-hill New York, 2000.

Md Mobashir Hasan Shandhi (M'17) received the BSc degree in Electrical and Electronics Engineering from Bangladesh University of Engineering & Technology (BUET), Dhaka, Bangladesh, in 2011 and the MSc degree in Electrical and Computer Engineering (ECE) from University of Utah, Salt Lake City, Utah, USA, in 2016. From 2011 to 2014, he was a lecturer at American International University – Bangladesh (AIUB), Dhaka, Bangladesh.

In 2016, he joined the department of ECE at Georgia Institute of Technology, where he is currently pursuing his Ph.D. degree. His research interests include biosensing, physiological monitoring, signal processing, machine learning, wearable biosensors, bioMEMS, and micromachining techniques to develop medical devices for clinically relevant applications and home monitoring of chronic diseases.

Sandeep Negi received the B.S. and M.S. degrees in physics from G.U., Dehradun, India, in 1996 and 1998; the M.Tech. degree in physics from IIT Delhi, New Delhi, India, in 2000; and the Ph.D. degree in electrical and computer engineering from the University of Utah, Salt Lake City, UT, USA, in 2009. From 2001 to 2004, he was with a semiconductor company in Singapore. From 2009 to 2012, and since 2015, he has been with a biomedical company in Salt Lake City. From 2012 to 2015, he was a Research Assistant Professor of electrical and computer engineering at the University of Utah. Since 2016, he has been an Adjunct Associate Professor of electrical and computer engineering with the University of Utah. In 2016, Dr. Negi co-founded Electrode Business (EB) which is a sister company of Blackrock Microsystems. His primary research interest includes biomaterials and the design, fabrication, and testing of implantable BioMEMS devices.